International Journal of Solids and Structures 195 (2020) 28–42

Contents lists available at ScienceDirect

International Journal of Solids and Structures

journal homepage: www.elsevier.com/locate/ijsolstr

On postbuckling mode distortion and inversion of nanostructures due to surface roughness

M. Shaat[a,*], S. Emam[b,c], S. Faroughi[d], U. Javed[e,f]

[a] Mechanical Engineering Department, Abu Dhabi University, P.O.BOX 1790, Al Ain, United Arab Emirates
[b] Faculty of Engineering, Zagazig University, Zagazig 44519, Egypt
[c] Department of Mechanical Engineering, American University of Sharjah, PO Box 26666, Sharjah, United Arab Emirates
[d] Faculty of Mechanical Engineering, Urmia University of Technology, Urmia, Iran
[e] Department of Mechanical Engineering, The University of Lahore, 1 km Raiwind Road, Lahore 53700, Pakistan
[f] Department of Engineering, American University of Iraq Sulaimani (AUIS), Sulaimania 46001, Iraq

ARTICLE INFO

Article history:
Received 8 April 2019
Revised 18 January 2020
Accepted 6 March 2020
Available online 17 March 2020

Keywords:
Postbuckling of beams
Surface roughness
Mode inversion
Mode distortion
Mode localization

ABSTRACT

In this paper, we investigate the surface roughness-dependence of buckling of beam-nanostructures. A new variational formulation of buckling of Euler-Bernoulli rough beams is developed based on the Hamilton's principle. The equation of motion of the beam is obtained with a coupling term that depends on the beam surface roughness. Exact solutions are derived for the buckling configurations and the pre-buckling and postbuckling vibrations of simply supported structures. The derived solutions are used to comprehensively explain influence of surface roughness on buckling characteristics of micro/nano-beams. We reveal that the buckling configurations and postbuckling mode shapes are distorted due to surface roughness. Thus, the beam with a rough surface may exhibit a localized buckling configuration where the buckling energy is confined over a small portion of the beam. In addition, the postbuckling mode shape of simply supported beams with rough surfaces is applied load-dependent. We report a value of the applied axial load at which the postbuckling mode shape is completely distorted, and the beam exhibits a mode shape that is identical to its buckling configuration but with a different amplitude. For the first time, we reveal a postbuckling mode inversion due to surface roughness. We demonstrate that the postbuckling mode shape starts to exhibit an inverted form of its original shape at high load values. The findings presented in this study highlight new insights into buckling characteristics of micro/nano-beams.

1. Introduction

There is a growing interest in developing advanced materials and structures (e.g., micro/nano-beams) with the capability of detecting micro/nano-scale phenomena. When it comes to measurement techniques, micro/nano beams are being utilized as needles or probes for atomic force microscopes to measure the size dependence of the elastic modulus, buckling, strength, and hardness of micro/nano-sized materials (Wu et al. 2001). In addition, the implementation of micro/nano beams in general extends to sensors and actuators for medicine, such as the mass detection of biological cells and viruses (Gupta et al., 2004; Johnson et al., 2006; Lu et al., 2012; Shaat and Abdelkefi, 2016a) or nano-drug carriers needed for healing tumor cells (Liu et al., 2012). Given the aforementioned applications of micro/nano-beams, new insights into the mechanics of micro/nano-beams are developed in the current work. Specifically, a nano-beam with a rough surface is modeled, and its buckling characteristics are deciphered.

To foster the design of nanomaterials for commercial and public use, advanced models of mechanics of nanomaterials and nanostructures are needed. Whereas models of molecular mechanics are accurate and can reveal many nano-scale phenomena, these models are not preferred when it comes to the mechanics-based design of materials. The computational cost of the molecular mechanics is relatively high, and it is computationally difficult when used to model the mechanics of complex nanostructures (Jain et al., 1993; Shaat and Abdelkefi, 2017). In contrast, models that treat the material as a continuum would be preferred to give a simple tool to design and engineer materials for practical implementations. However, the classical concept of continuum mechanics breaks down when used to model the mechanics of nanomaterials and nanostructures. The mechanics of nanomaterials depends on nano-scale phenomena, and the classical mechanics lacks the measures needed to capture these phenomena (Shaat et al., 2012;

* Corresponding author.
E-mail addresses: mohamed.i@adu.ac.ae, shaatscience@yahoo.com (M. Shaat).

https://doi.org/10.1016/j.ijsolstr.2020.03.007
0020-7683/

Shaat, 2016b). The classical mechanics gives no considerations for neither the discrete structure of the material nor the shape and/or the size of its microstructure (Shaat, 2018b; Mindlin, 1964). Therefore, advanced models of continuum mechanics that incorporate measures of the nano-scale phenomena are needed.

Several advanced models of continuum mechanics have been developed to capture many of the non-traditional phenomena of nanomaterials. Some of the non-traditional phenomena are related to material microstructure, while others stem from the material surface. When it comes to the microstructure, a nonlocal model or a micromorphic model is needed. The influence of the long-range interatomic interactions on the material mechanics can be captured using a nonlocal model. For example, effects of interatomic interactions on pull-in stability and frequencies of electrostatic nanoswitches (Gholami et al., 2015) and nanoactuators (Sedighi et al., 2015; Najar et al., 2015; Rahaeifard et al., 2011; Kong, 2013; Shaat and Mohamed, 2014; Kahrobaiyan et al., 2015; Rahaeifard and Ahmadian, 2015), vibrations of graphene and carbon nanotubes (Aydogdu and Arda, 2016; Shaat and Faroughi, 2019), and buckling of micro/nano-beams (Thai, 2012; Nateghi et al., 2012; Simsek and Reddy, 2013) have been discussed in various studies using one of the nonlocal theories like Eringen's nonlocal elasticity (Thai, 2012; Shaat and Faroughi, 2019), modified couple stress theory (Nateghi et al., 2012; Simsek and Reddy, 2013) or modified strain gradient theory (Akgöz and Civalek, 2011; Lazopoulos and Lazopoulos, 2010) and the surface elasticity (Shaat and Abdelkefi, 2018). When the mechanics of the material strongly depends on microscopic fields, e.g. micro-strains and micro-rotations, a micromorphic model is needed (Shaat, 2018a; Madeo et al., 2015; Madeo and Neff, 2017). For instance, micromorphic models were developed to reveal the wave propagation and bandgap characteristics of phononic materials and acoustic metamaterial (Shaat, 2018a; Madeo et al., 2015). As for the surface, the mechanics of a nanomaterial can be altered considerably due to a slight change in its surface mechanical, chemical, or geometrical properties (Eremeyev, 2016; Allahyari and Fadaee, 2016; Shaat et al., 2014; Shaat and Mohamed, 2014). For example, under zero-loading conditions, a material may exhibit a geometrical defect due to a residual surface stress field (Wang and Zhao, 2009; Zang and Zhao, 2012; Shaat, 2018b). In addition, it was observed that the dynamics of nanoresonators strongly depend on the roughness of their surfaces (Yoon et al., 2013; Palasantzas, 2007).

Since the current work focuses on buckling of beams with rough surfaces, it is important to note that models have been developed to relate the material mechanics to its surface. Early investigations on surface phenomenon can be attributed to Laplace (Laplace, 1805; Laplace, 1806), Young (Young, 1805) and Poisson (Poisson, 1831), where they developed the fluid mechanics in accordance to its surface tension. Then, Gibbs (Gibbs, 1928) extended the idea of the surface tension to solid mechanics. Later after, Gurtin and Murdoch (Gurtin and Murdoch, 1975a,b) developed a surface elasticity model that considers large deformation of the surface due to its residual stresses. Gurtin-Murdoch model is nothing but a solid material with an elastic membrane of a zero-thickness attached on its surface. It considers the stress resultants acting on the membrane as a surface stress field. The way Gurtin-Murdoch model approached the surface elasticity made it particularly interesting for researchers and found applications in investigating size dependence mechanics of nanostructures (e.g., Duan et al., 2008; Javili et al., 2012; Wang et al., 2011). The model was then generalized for different applications (Javili et al., 2013; Javili, 2012; Podio-Guidugli and Caffarelli, 1990; Povstenko, 2013; Šilhavý, 2013; Rubin and Benvenisten, 2004; Lurie and Belov, 2014). Recently, Shaat (Shaat, 2018c) developed a generalized model of surface integrity effects on the mechanics of solid materials. Unlike formal models of surface elasticity, which assume nominal surfaces, the surface integrity model (Shaat, 2018c) treats the material with an engineering surface. An engineering surface is featured with a surface texture, i.e. surface roughness and waviness, and an altered layer between the free surface and the material bulk. Using the surface integrity model, it was revealed that frequencies of micro/nano-beams would increase or decrease, and micro/nano-beams would exhibit mode localization due to surface roughness (Shaat, 2018b; 2018d; Shaat and Faroughi, 2018). Moreover, it was demonstrated that the surface integrity model outweighs Gurtin-Murdoch model in incorporating details which show that surface energy depends not only on the surface stress but also the surface texture (Shaat, 2018b; 2018c).

Buckling is one of the important phenomena that beam-column structures exhibit when subjected to compressive loads. A beam-column structure would buckle (i.e., transversely deform) to a certain configuration when subjected to an axial compressive load that exceeds a certain limit (known as the critical buckling load). The critical buckling load depends on the geometry and the material of the beam structure. Understanding the conditions at which micro/nano-beams would buckle are important to design advanced materials. For instance, an auxetic metamaterial (an auxetic material possesses a negative Poisson's ratio) was 3D-printed with a special topology that promotes buckling of the strips of the unit cell. Different buckling configurations of the strips were obtained at different axial loads to give a metamaterial with a tunable Poisson's ratio. In addition, the dynamics of buckled micro/nano-beams would reveal nontraditional phenomena, which would give rise to advanced designs of materials when explored. Therefore, great efforts have been devoted to explore the buckling characteristics of micro/nano-beams (Wang et al., 2006; Akoz and Civolek, 2011; Nateghi et al., 2012; Simsek and Yurtcu, 2013; Ghannadpour et al., 2013; Emam, 2013; Mohammad-Abadi and Daneshmehr, 2014; Chaht et al., 2015; Niknam and Aghdam, 2015; Li and Hu, 2015; Nejad et al., 2016; Khorshidi et al., 2016; Shaat and Abdelkefi, 2018, Shaefei and Kazmi, 2017; Xu et al., 2017).

Here, the influence of the surface roughness on buckling characteristics of micro/nano-beams is comprehensively explained, for the first time. A new model of beams with rough surfaces is developed. This model is pioneered based on the surface integrity model (Shaat, 2018c). The obtained model is then analytically solved. The exact buckling configurations are determined depending on the beam surface roughness. In addition, the surface roughness-dependence of the load at which beam would buckle to a certain configuration (i.e., critical buckling load) is interpreted. Moreover, the free vibrations of buckled beams are interpreted to explore the influence of the surface roughness on the postbuckling frequencies and mode shapes. A comprehensive discussion on the inversion of the postbuckling mode shape due to surface roughness is provided. The findings of the present study are of significant importance to the mechanics-based design of micro/nano-beams with rough surfaces for various applications. Nanobeams with graded rough surfaces have been made to give advanced fog collectors and water conveyors (Xing et al., 2017). In addition, the surface roughness can be tailored to give nanobeams with meta-surfaces (Hsiao et al., 2017).

2. Formulation

This study investigates the buckling characteristics of beam nanostructures with rough surfaces. To this end, a beam-column under an axial compressive load is modeled based on the surface integrity model (Shaat, 2018c). The nanobeam is modeled as a von-Karman geometrically nonlinear Euler-Bernoulli beam that occupies a material bulk of volume (V) and a surface (S). The beam surface is rough with a surface roughness profile ($\mathcal{R}(x)$). The beam

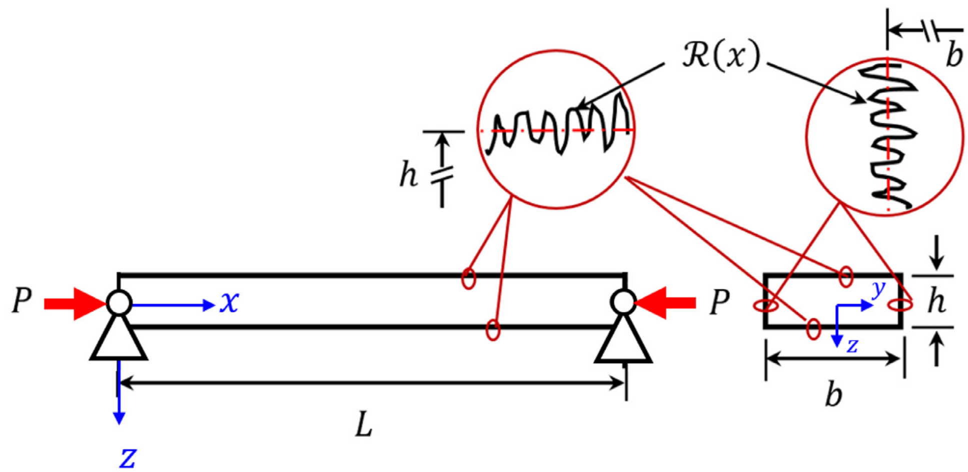

Fig. 1. A schematic of a simple supported beam with a rough surface. The beam is featured with a surface roughness with a profile function $\mathcal{R}(x)$ and subjected to an axial compressive load (P). L, b, and h denote the length, width, and thickness of the nominal beam, respectively. All surfaces of the beam are rough.

is simply supported and subjected to a compressive axial load P, as shown in Fig. 1. Therefore, the displacement field (u_i, where the subscript i denotes x, y, and z) of a point, $\mathbf{x} = (x, y, z)$, belongs to the beam's axis is defined as follows:

$$u_x(x,z,t) = u(x,t) - z\nabla w(x,t), \quad u_y = 0, \quad \text{and}\, u_z(x,z,t) = w(x,t) \tag{1}$$

where $u(x, t)$ and $w(x, t)$ are the axial displacement and the lateral deflection of the beam, respectively. $\nabla^m = \frac{\partial^m}{\partial x^m}$ is a gradient operator.

According to Eq. (1), the non-zero strain component ε_{xx} – accounting for the von-Karman's geometrical nonlinearity – is obtained as

$$\varepsilon_{xx}(x,t) = \left(\nabla u(x,t) + \frac{1}{2}(\nabla w(x,t))^2\right) - z\nabla^2 w(x,t) \tag{2}$$

Hence, neglecting the Poisson's ratio effects, the non-zero stress component for an isotropic elastic beam has the form

$$\sigma_{xx}(x,t) = E\left(\nabla u(x,t) + \frac{1}{2}(\nabla w(x,t))^2 - z\nabla^2 w(x,t)\right) \tag{3}$$

where E is the Young's modulus of the beam material.

The equation of motion of a nanobeam with a rough surface can be derived based on the Hamilton's principle

$$\int_0^t (\delta T - \delta U + \delta Q)dt = 0 \tag{4}$$

where δT, δU, and δQ are, respectively, the first variations of the kinetic energy, strain energy, and work done by the non-conservative forces.

For the considered nanobeam, these quantities can be expressed as follows:

$$\delta U = \int_{V(x)} \sigma_{xx}(x,t)\delta\varepsilon_{xx}(x,t)dV \tag{5}$$

$$\delta T = -\int_{V(x)} \rho\ddot{w}(x,t)\delta w(x,t)dV \tag{6}$$

$$\delta Q = \int_{\Gamma} P\delta u_x(x,t)dS \tag{7}$$

where ρ is the mass density of the beam material. The dot refers to a time derivative. It should be mentioned that the axial and rotatory inertias are neglected.

By substituting Eqs. (5)–(7) into Eq. (4), the equation of motion of nanobeams with rough surfaces can be obtained in terms of the stress resultants, as follows:

$$\nabla N_x(x,t) = 0 \tag{8}$$

$$\nabla^2 M_x(x,t) + \nabla(N_x(x,t)\nabla w(x,t)) - m(x)\ddot{w}(x,t) = 0 \tag{9}$$

where

$$m(x) = \int_{A(x)} \rho dA = 4\rho\left(\frac{b}{2} + \mathcal{R}(x)\right)\left(\frac{h}{2} + \mathcal{R}(x)\right) \tag{10}$$

where b and h are the beam's width and thickness, respectively. It should be noted that $\mathcal{R}(x)$ represents the deviations of the asperities of the surface roughness measured from the nominal surface of the beam, as shown in Fig. 1.

Because the beam is subjected to an axial compressive load (P), the resultant axial force N_x can be defined as follows:

$$N_x(x,t) = \int_{A(x)} \sigma_{xx}(x,t)dA - P = S(x)\left(\nabla u(x,t) + \frac{1}{2}(\nabla w(x,t))^2\right) - P \tag{11}$$

and the resultant moment M_x can be written as follows:

$$M_x(x,t) = \int_{A(x)} z\sigma_{xx}(x,t)dA = -D(x)\frac{\partial^2 w(x,t)}{\partial x^2} \tag{12}$$

where

$$D(x) = EI(x)$$
$$S(x) = 4E\left(\frac{b}{2} + \mathcal{R}(x)\right)\left(\frac{h}{2} + \mathcal{R}(x)\right) \tag{13}$$

with

$$I(x) = \int_{A(x)} z^2 dA = \frac{4}{3}\left(\frac{b}{2} + \mathcal{R}(x)\right)\left(\frac{h}{2} + \mathcal{R}(x)\right)^3 \tag{14}$$

where b and h are the beam width and thickness, respectively.

By substituting Eq. (12) into Eq. (9) and noting that N_x is constant as per Eq. (8), the equation of motion becomes

$$D(x)\nabla^4 w(x,t) + K(x)\nabla^3 w(x,t) + (B(x) - N_x)\nabla^2 w(x,t) + m(x)\ddot{w}(x,t) = 0 \tag{15}$$

where

$$K(x) = 2\frac{dD(x)}{dx}$$

$$B(x) = \frac{d^2D(x)}{dx^2} \tag{16}$$

For simply supported beams, the following boundary conditions are employed:

$$\begin{aligned} &w(0,t) = 0 \text{ and } w(L,t) = 0 \\ &D(0)\nabla^2 w(0,t) = 0 \text{ and } D(L)\nabla^2 w(L,t) = 0. \end{aligned} \tag{17}$$

where L is the beam length.

It follows from Eq. (15) that surface roughness would strongly influence the deflection of the beam. The coefficients in Eq. (15) depend on the surface roughness profile, $\mathcal{R}(x)$. The profile function, $\mathcal{R}(x)$, can be determined upon inspecting the surface of the beam using an atomic force microscope (Shaat, 2018d). The microscope usually gives an image of the inspected surface. Using an image analysis software, e.g., Gwyddion Software (Shaat, 2018d), the profile of the surface roughness is obtained. Usually, the profile of surface roughness is very random. Therefore, the roughness average is the commonly used measure of surface roughness in various engineering applications. Following the approach proposed by Shaat (Shaat, 2018c), the average of the surface roughness and the average slope of the surface roughness are defined as

$$\begin{aligned} R_a &= \langle \mathcal{R}(x) \rangle = \frac{1}{L}\int_0^L |\mathcal{R}(x)| dx \\ R_S &= \langle d\mathcal{R}(x)/dx \rangle = \frac{1}{L}\int_0^L \left| \frac{d\mathcal{R}(x)}{dx} \right| dx \end{aligned} \tag{18}$$

where R_a is the average surface roughness, and R_S is the average slope of the surface roughness. It should be mentioned that the higher-order gradients of the surface roughness are neglected (Shaat, 2018c).

Utilizing the average parameters of the surface roughness, R_a and R_S, defined in Eq. (18), the equation of motion and the boundary conditions can be written in the form:

$$D\nabla^4 w(x,t) + K\nabla^3 w(x,t) + (B - N_x)\nabla^2 w(x,t) + m\ddot{w}(x,t) = 0 \tag{19}$$

$$\begin{aligned} &w(0,t) = 0 \quad \text{and } w(L,t) = 0 \\ &\nabla^2 w(0,t) = 0 \quad \text{and } \nabla^2 w(L,t) = 0 \end{aligned} \tag{20}$$

where

$$\begin{aligned} &D = EI \text{ , i.e., } I = \frac{4}{3}\left(\frac{b}{2} + R_a\right)\left(\frac{h}{2} + R_a\right)^3 \\ &K = \frac{8}{3}ER_S\left[3\left(\frac{b}{2} + R_a\right)\left(\frac{h}{2} + R_a\right)^2 + \left(\frac{h}{2} + R_a\right)^3\right] \\ &B = 8ER_S^2\left[\left(\frac{b}{2} + R_a\right)\left(\frac{h}{2} + R_a\right) + \left(\frac{h}{2} + R_a\right)^2\right] \\ &m = 4\rho\left(\frac{b}{2} + R_a\right)\left(\frac{h}{2} + R_a\right) \\ &N_x(x,t) = S\left(\nabla u(x,t) + \frac{1}{2}(\nabla w(x,t))^2\right) - P \\ &S = 4E\left(\frac{b}{2} + R_a\right)\left(\frac{h}{2} + R_a\right) \end{aligned} \tag{21}$$

It should be noted that N_x is constant according to Eq. (8), and it expresses the resultant axial force induced in the beam. Here, the beam ends are considered at a fixed distance a part. Therefore, the transverse deflection of the beam creates a midplane stretching, which is modeled based on the von-Karman's geometrical nonlinearity, that is equivalent to an induced stretching force. As a result, the resultant axial force can be expressed as follows (Nayfeh and Emam, 2008)

$$N_x(x,t) = \frac{S}{2L}\int_0^L (\nabla w(x,t))^2 dx - P \tag{22}$$

The substitution of Eq. (22) into Eq. (19) yields

$$\begin{aligned} &D\nabla^4 w(x,t) + K\nabla^3 w(x,t) + \left(B + P - \frac{S}{2L}\int_0^L (\nabla w(x,t))^2 dx\right) \\ &\quad \nabla^2 w(x,t) + m\ddot{w}(x,t) = 0 \end{aligned} \tag{23}$$

The proposed model is unique and novel. It follows from Eq. (23) that the surface integrity model shows that the beam buckling depends on the stiffnesses (K, B, and S), which model effects of the surface texture on the beam deflection. The proposed model reduces to the classical model proposed by Nayfeh and Emam (2008) when $R_a \to 0$ and $R_S \to 0$.

Eq. (23) governs the transverse deflection of a beam under a compressive axial loading where the beam ends are assumed at a fixed distance apart. An application where a mechanical load is applied at one end that is allowed to slide axially towards the other end is outside the scope of the proposed model given by Eq. (23). In addition, Eq. (23) represents the geometric nonlinearity due to the midplane stretching according to von Karman's approximation. Thus, the model can handle deformations within the shallow-arch assumptions where small strain and moderate rotation approximations are adopted.

For the sake of study and without loss of generality, the derived equation of motion and boundary conditions are rewritten in a normalized form utilizing the following nondimensional parameters:

$$W(X,T) = \frac{w(x,t)}{r}, \; X = \frac{x}{L}, \; T = t\sqrt{\frac{D}{mL^4}} \tag{24}$$

where r is the cross-section radius of gyration that is equal to $h/\sqrt{12}$ for a rectangular cross section.

This gives Eq. (23) in the form:

$$\nabla^4 W(X,T) + \alpha\nabla^3 W(X,T) + \beta\nabla^2 W(X,T) + \ddot{W}(X,T) = 0 \tag{25}$$

where

$$\begin{aligned} \alpha &= \frac{KL}{D} = \frac{12R_SL}{h + 2R_a} + \frac{4R_SL}{b + 2R_a} \\ \beta &= \frac{(B + P)L^2}{D} - \frac{Sh^2}{24D}\int_0^1 (\nabla W(X,T))^2 dX \end{aligned} \tag{26}$$

and the boundary conditions (Eq. (20)) in the form:

$$\begin{aligned} &W(0,T) = 0 \text{ and } W(1,T) = 0 \\ &\nabla^2 W(0,T) = 0 \text{ and } \nabla^2 W(1,T) = 0 \end{aligned} \tag{27}$$

Eq. (25) contains a coupling term with a coefficient α that depends on the beam surface roughness. As long as the coefficient of the coupling term is significant, the beam exhibits non-classical buckling mode shapes, as it will be explained later. It follows from Eq. (26) that $\lim_{R_S \to 0} \alpha = 0$. Meanwhile, as the cross-sectional height h and width b decrease, the parameter α increases, and the effect of the coupling term becomes significant. On the other hand, the effect of the surface roughness is generally insignificant as the beam is with a macroscopic size.

Next, exact solutions of the buckling configurations and prebuckling and postbuckling frequencies and mode shapes are derived.

3. Exact analytical solution

Here, we present an exact solution of the derived equation of motion that governs the buckling of nanobeams with rough surfaces. The exact buckling configurations and the exact eigenvalues and mode shapes of the beam in the prebuckling and postbuckling regimes are derived. To this end, the nondimensional beam deflection is represented as follows:

$$W(X,T) = \eta(X) + v(X,T) \tag{28}$$

where $\eta(X)$ represents the static buckling configuration, and $v(X, T)$ is a dynamic disturbance applied to the beam at its buckling configuration $\eta(X)$.

The substitution of Eq. (28) into Eq. (25) gives

$$\begin{aligned}
&\nabla^4\eta(X) + \alpha\nabla^3\eta(X) + \left(\beta_s - \frac{Sh^2}{24D}\int_0^1 (\nabla v(X,T))^2 dX \right.\\
&\left. - \frac{Sh^2}{12D}\int_0^1 (\nabla\eta(X)\nabla v(X,T))dX\right)\nabla^2\eta(X)\\
&+ \nabla^4 v(X,T) + \alpha\nabla^3 v(X,T)\\
&+ \left(\beta_s - \frac{Sh^2}{24D}\int_0^1 (\nabla v(X,T))^2 dX \right.\\
&\left. - \frac{Sh^2}{12D}\int_0^1 (\nabla\eta(X)\nabla v(X,T))dX\right)\nabla^2 v(X,T)\\
&+ \ddot{v}(X,T) = 0
\end{aligned} \tag{29}$$

where

$$\beta_s = \frac{(B+P)L^2}{D} - \frac{Sh^2}{24D}\int_0^1 (\nabla\eta(X))^2 dX \tag{30}$$

and into Eq. (27) gives the boundary conditions:

$$\begin{aligned}
&\eta(0) + v(0,T) = 0 \quad \text{and}\ \eta(1) + v(1,T) = 0\\
&\nabla^2\eta(0) + \nabla^2 v(0,T) = 0 \ \text{and}\ \nabla^2\eta(1) + \nabla^2 v(1,T) = 0
\end{aligned} \tag{31}$$

It should be mentioned that the nonlinear terms in Eq. (29) are geometrical nonlinearities because of the beam axial stretching.

3.1. Static analysis: buckling configuration

The different buckling configurations of the beam can be determined by solving the underlying static problem of the proposed model. Therefore, Eqs. (29) and (31) are rewritten after dropping the time dependent terms, as follows:

$$\nabla^4\eta(X) + \alpha\nabla^3\eta(X) + \beta_s\nabla^2\eta(X) = 0 \tag{32}$$

$$\begin{aligned}
&\eta(0) = 0 \quad \text{and} \quad \eta(1) = 0\\
&\nabla^2\eta(0) = 0 \quad \text{and} \quad \nabla^2\eta(1) = 0
\end{aligned} \tag{33}$$

where α and β_s are defined in Eqs. (26) and (30), respectively.

A general solution of Eq. (32) is obtained in the form

$$\eta(X) = A_1 + A_2 X + e^{-\frac{\alpha X}{2}}(A_3\cos(kX) + A_4\sin(kX)) \tag{34}$$

where $k = \frac{1}{2}\sqrt{4\beta_s - \alpha^2}$.

By substituting Eqs. (34) into (33), the following equations are obtained:

$$\begin{bmatrix} 1 & 0 & 1 & 0\\ 0 & 0 & \frac{1}{4}(\alpha^2 - 4k^2) & -\alpha k\\ 1 & 1 & e^{-\frac{\alpha}{2}}\cos(k) & e^{-\frac{\alpha}{2}}\sin(k)\\ 0 & 0 & d_1 & d_2 \end{bmatrix} \begin{Bmatrix} A_1\\ A_2\\ A_3\\ A_4 \end{Bmatrix} = 0 \tag{35}$$

where

$$d_1 = e^{-\frac{\alpha}{2}}\left(\frac{1}{4}(\alpha^2 - 4k^2)\cos(k) + \alpha k\sin(k)\right)$$

$$d_2 = e^{-\frac{\alpha}{2}}\left(-\alpha k\cos(k) + \frac{1}{4}(\alpha^2 - 4k^2)\sin(k)\right)$$

The determinant of the coefficient matrix of Eq. (35) gives

$$e^{-\frac{\alpha}{2}}(\alpha^2 + 4k^2)\sin(k) = 0 \tag{36}$$

According to Eq. (36), either

$$\alpha^2 + 4k^2 = 0 \tag{37}$$

or

$$\sin(k) = 0 \tag{38}$$

The condition given by Eq. (37), is rejected because it gives the buckling configuration independent of the applied axial load. The other condition in Eq. (38) gives

$$k = n\pi$$

and hence

$$\beta_s = (n\pi)^2 + \frac{\alpha^2}{4} \tag{39}$$

where n = 1, 2, 3, … refers to the buckling modes.

Solving the first three equations of (35), the nth buckling mode can be defined as follows:

$$\begin{aligned}
\eta_n(X) = {}& \frac{4n\pi\alpha}{\alpha^2 - (2n\pi)^2}A_4\Big[-1 + \left(1 - \cos(n\pi)e^{-\frac{\alpha}{2}}\right)X\\
&+ e^{-\frac{\alpha}{2}X}\cos(n\pi X)\Big] + e^{-\frac{\alpha}{2}X}\sin(n\pi X)
\end{aligned} \tag{40}$$

where A_4 can be set equal to one. This mode shape reduces to the classical buckling mode of simply supported beams when the coefficient α is set equal to zero.

The value of the compressive load that is required to initiate the beam buckling into the nth buckling configuration (i.e., nth buckling mode, $\eta_n(X)$) can be obtained by equating the critical value of β_s in Eq. (39) to its linear part in Eq. (30) as follows:

$$P_{cr} = \frac{D\left(n^2\pi^2 + \frac{\alpha^2}{4}\right)}{L^2} - B \tag{41}$$

The buckling amplitude in the postbuckling domain in terms of the applied axial load and the beam parameters can be obtained by substituting Eqs. (39) and (40) into Eq. (30) and solving the resulted equation for A_4. This gives the buckling mode in the form

$$\begin{aligned}
\eta_n(X) = {}& \xi_n\Big(-1 + \left(1 - e^{-\frac{\alpha}{2}}\cos(n\pi)\right)X\\
&\mp e^{-\frac{\alpha}{2}X}\left[\cos(n\pi X) \pm \frac{\alpha^2 - 4(n\pi)^2}{4\alpha n\pi}\sin(n\pi X)\right]\Big)
\end{aligned} \tag{42}$$

where ξ_n is a constant defined as follows:

$$\xi_n = \sqrt{\frac{24D}{Sh^2\left(\bar{a}(n\pi)^4 + \bar{b}(n\pi)^2 + \bar{c}\right)}\left(\frac{(B+P)L^2}{D} - n^2\pi^2 - \frac{\alpha^2}{4}\right)} \tag{43}$$

where

$$\begin{aligned}
\bar{a} &= \frac{1 - e^{-\alpha}}{2\alpha^3}\\
\bar{b} &= \frac{3}{4}\frac{(1 - e^{-\alpha})}{\alpha}\\
\bar{c} &= 2\cos(k)e^{-\frac{\alpha}{2}} - \left(\frac{5}{32}\alpha + 1\right)e^{-\alpha} + \frac{5\alpha}{32} - 1
\end{aligned} \tag{44}$$

Eqs. (40)–(44) give the critical buckling loads and the buckling configuration as functions of the beam surface texture. Effects of the surface texture are captured via α and B, which are defined depending on the beam surface roughness parameters (R_a and R_S). When $\alpha \to 0$ and $B \to 0$, the model reduces to the one of the buckling of classical beams (Nayfeh and Emam, 2008).

3.2. Free-vibration analysis

3.2.1. Prebuckling

The free vibration of the prebuckling response is governed by Eqs. (29)–(31), where the static configuration $\eta(X)$ is set equal to zero, as follows:

$$\nabla^4 v(X,T) + \alpha\nabla^3 v(X,T) + \varrho\nabla^2 v(X,T) - \left(\frac{Sh^2}{24D}\int_0^1 (\nabla v(X,T))^2 dX\right)\nabla^2 v(X,T) + \ddot{v}(X,T) = 0 \tag{45}$$

$$v(0,T) = 0 \text{ and } v(1,T) = 0$$
$$\nabla^2 v(0,T) = 0 \text{ and } \nabla^2 v(1,T) = 0 \tag{46}$$

where

$$\varrho = \frac{(B+P)L^2}{D} \tag{47}$$

The function $v(X, T)$ is assumed harmonic in the form

$$v(X,T) = \phi(X)e^{i\omega T} \tag{48}$$

where ω denotes a natural frequency, and $\varphi(X)$ represents its corresponding mode shape.

For the free vibration analysis of the unbuckled beam, the nonlinear term in Eq. (45) is eliminated. Eq. (48) is substituted into Eqs. (45) and (46) to give

$$\nabla^4\phi(X) + \alpha\nabla^3\phi(X) + \varrho\nabla^2\phi(X) - \omega^2\phi(X) = 0 \tag{49}$$

$$\phi(0) = 0 \text{ and } \phi(1) = 0$$
$$\nabla^2\phi(0) = 0 \text{ and } \nabla^2\phi(1) = 0 \tag{50}$$

The general solution of Eq. (49) can be obtained in the following form:

$$\phi(X) = B_r e^{\lambda_r X} \tag{51}$$

where B_r and λ_r are constants to be determined. The substitution of Eq. (51) into Eq. (49) yields the following characteristics equation for λ:

$$\lambda^4 + \alpha\lambda^3 + \varrho\lambda^2 - \omega^2 = 0 \tag{52}$$

Demanding that the mode shape $\varphi(x)$ in Eq. (51) satisfies the boundary conditions given by Eq. (50), the following equations are obtained:

$$\sum_{r=1}^{4} B_r = 0,\ \sum_{r=1}^{4} B_r\lambda_r^2 = 0,\ \sum_{r=1}^{4} B_r e^{\lambda_r} = 0,\ \sum_{r=1}^{4} B_r\lambda_r^2 e^{\lambda_r} = 0 \tag{53}$$

The prebuckling natural frequencies can be then determined by solving the following equation:

$$\det\begin{bmatrix} 1 & 1 & 1 & 1 \\ \lambda_1^2 & \lambda_2^2 & \lambda_3^2 & \lambda_4^2 \\ e^{\lambda_1} & e^{\lambda_2} & e^{\lambda_3} & e^{\lambda_4} \\ \lambda_1^2 e^{\lambda_1} & \lambda_2^2 e^{\lambda_2} & \lambda_3^2 e^{\lambda_3} & \lambda_4^2 e^{\lambda_4} \end{bmatrix} = 0 \tag{54}$$

Solving the first three equations in (Eq. (54)) gives the constants, B_r, in the form:

$$B_3 = -B_1\frac{\delta_1}{\delta_2}$$
$$B_4 = \frac{1}{\lambda_4^2 - \lambda_2^2}\left(-B_1\lambda_1^2 + \lambda_2^2(B_1 + B_3) - B_3\lambda_3^2\right)$$
$$B_2 = -B_1 - B_3 - B_4$$
$$\delta_1 = e^{\lambda_1} - e^{\lambda_2} + \left(\frac{\lambda_1^2 - \lambda_2^2}{\lambda_4^2 - \lambda_2^2}\right)\left(e^{\lambda_2} - e^{\lambda_4}\right)$$
$$\delta_2 = e^{\lambda_3} - e^{\lambda_2} + \left(\frac{\lambda_3^2 - \lambda_2^2}{\lambda_4^2 - \lambda_2^2}\right)\left(e^{\lambda_2} - e^{\lambda_4}\right) \tag{55}$$

3.2.2. Postbuckling

To investigate the free vibration of the buckled beam about a given buckling configuration $\eta(X)$, the nonlinear terms of $v(X, T)$ in Eq. (29) are dropped to give:

$$\nabla^4\eta(X) + \alpha\nabla^3\eta(X) + \beta_s\nabla^2\eta(X) + \nabla^4 v(X,T) + \alpha\nabla^3 v(X,T) + \beta_s\nabla^2 v(X,T) + \ddot{v}(X,T) = \left(\frac{Sh^2}{12D}\int_0^1 (\nabla\eta(X)\nabla v(X,T))dX\right)\nabla^2\eta(X) \tag{56}$$

where β_s is defined by Eq. (39).

Assuming a harmonic response for $v(X, T)$ in the form

$$v(X,T) = \psi(X)e^{i\omega T} \tag{57}$$

where ω is the postbuckling natural frequency, and $\psi(X)$ is the postbuckling mode shape.

According to Eq. (32), the first four terms of Eq. (56) vanish. The substitution of Eq. (57) into Eq. (56) gives

$$\nabla^4\psi(X) + \alpha\nabla^3\psi(X) + \beta_s\nabla^2\psi(X) - \omega^2\psi(X) = \left(\frac{Sh^2}{12D}\int_0^1 (\nabla\eta(X)\nabla\psi(X))dX\right)\nabla^2\eta(X) \tag{58}$$

According to Eqs. (33) and (57), the boundary conditions (31) can be rewritten as follows

$$\psi(0) = 0 \text{ and } \psi(1) = 0$$
$$\nabla^2\psi(0) = 0 \text{ and } \nabla^2\psi(1) = 0 \tag{59}$$

A general solution of Eq. (58) is obtainable in the form

$$\psi(X) = \psi_h(X) + \psi_P(X) \tag{60}$$

where $\psi_h(X)$ is the homogenous solution, and $\psi_P(X)$ is the particular solution.

The substitution of Eq. (60) into Eq. (58) gives

$$\nabla^4\psi_h(X) + \alpha\nabla^3\psi_h(X) + \beta_s\nabla^2\psi_h(X) - \omega^2\psi_h(X) + \nabla^4\psi_P(X) + \alpha\nabla^3\psi_P(X) + \beta_s\nabla^2\psi_P(X) - \omega^2\psi_P(X) = \left(\frac{Sh^2}{12D}\int_0^1 (\nabla\eta(X)(\nabla\psi_h(X) + \nabla\psi_P(X)))dX\right)\nabla^2\eta(X) \tag{61}$$

Because the integration in the right hand side of the equation is constant, the homogeneous solution can be determined by solving the following ordinary differential equation:

$$\nabla^4\psi_h(X) + \alpha\nabla^3\psi_h(X) + \beta_s\nabla^2\psi_h(X) - \omega^2\psi_h(X) = 0 \tag{62}$$

which is obtained in the form

$$\psi_h(X) = C_r e^{\lambda_r X} \tag{63}$$

where C_r are constants to be determined. λ_r are the roots of the following characteristics equation:

$$\lambda^4 + \alpha\lambda^3 + \beta_s\lambda^2 - \omega^2 = 0 \tag{64}$$

The particular solution can be obtained in the form

$$\psi_P(X) = C_5\nabla^2\eta(X) \tag{65}$$

where C_5 can be obtained to satisfy the following equation:

$$\nabla^4\psi_P(X) + \alpha\nabla^3\psi_P(X) + \beta_s\nabla^2\psi_P(X) - \omega^2\psi_P(X) = \left(\frac{Sh^2}{12D}\int_0^1 (\nabla\eta(X)(\nabla\psi_h(X) + \nabla\psi_P(X)))dX\right)\nabla^2\eta(X) \tag{66}$$

The substitution of Eq. (65) into Eq. (66) yields

$$C_5\nabla^2\left(\nabla^4\eta(X) + \alpha\nabla^3\eta(X) + \beta_s\nabla^2\eta(X)\right) - C_5\omega^2\nabla^2\eta(X) = \left(\frac{Sh^2}{12D}\int_0^1 (\nabla\psi_h(X)\nabla\eta(X))dX\right)\nabla^2\eta(X)$$

$$+C_5\left(\frac{Sh^2}{12D}\int_0^1\left(\nabla^3\eta(X)\nabla\eta(X)\right)dX\right)\nabla^2\eta(X) \quad (67)$$

The first term in Eq. (67) vanishes because of the static equilibrium condition (32). Therefore, Eq. (67) reduces to

$$\left(\frac{Sh^2}{12D}\int_0^1(\nabla\psi_h(X)\nabla\eta(X))dX\right)$$
$$+C_5\left(\omega^2+\frac{Sh^2}{12D}\int_0^1\left(\nabla^3\eta(X)\nabla\eta(X)\right)dX\right)=0 \quad (68)$$

$$\det\begin{bmatrix} 1 & 1 & 1 & 1 \\ \lambda_1^2-\frac{a_1}{\omega^2+\mathcal{H}}\nabla^4\eta(0) & \lambda_2^2-\frac{a_2}{\omega^2+\mathcal{H}}\nabla^4\eta(0) & \lambda_3^2-\frac{a_3}{\omega^2+\mathcal{H}}\nabla^4\eta(0) & \lambda_4^2-\frac{a_4}{\omega^2+\mathcal{H}}\nabla^4\eta(0) \\ e^{\lambda_1} & e^{\lambda_2} & e^{\lambda_3} & e^{\lambda_4} \\ \lambda_1^2e^{\lambda_1}-\frac{a_1}{\omega^2+\mathcal{H}}\nabla^4\eta(1) & \lambda_2^2e^{\lambda_2}-\frac{a_2}{\omega^2+\mathcal{H}}\nabla^4\eta(1) & \lambda_3^2e^{\lambda_3}-\frac{a_3}{\omega^2+\mathcal{H}}\nabla^4\eta(1) & \lambda_4^2e^{\lambda_4}-\frac{a_4}{\omega^2+\mathcal{H}}\nabla^4\eta(1) \end{bmatrix}=0 \quad (75)$$

According to Eqs. (63) and (68), C_5 can be obtained in the form

$$C_5=-\frac{\sum_{r=1}^4 a_rC_r}{\omega^2+\mathcal{H}} \quad (69)$$

where

$$a_r=\frac{Sh^2}{12D}\int_0^1\left(e^{\lambda_rX}\nabla\eta(X)\right)dX$$
$$\mathcal{H}=\frac{Sh^2}{12D}\int_0^1\left(\nabla^3\eta(X)\nabla\eta(X)\right)dX \quad (70)$$

The quantities are explicitly obtained in the form:

$$a_r=\mathcal{F}\xi_n(g_1\cos(n\pi)+g_2)$$
$$\mathcal{H}=\frac{Sh^2}{12D}\left(\frac{\xi_n^2}{512\alpha^3(n\pi)^2}\right)\left(\alpha^2+4(n\pi)^2\right)^3\left[\left(\alpha^2\cos(2n\pi)-\alpha^2+4(n\pi)^2\right)e^{-\alpha}-4(n\pi)^2\right]$$

where

$$g_1=4(n\pi)\left(4\lambda_r^2(n\pi)^2+\alpha^2\left(\lambda_r^2-4\lambda_r\right)+\alpha^3(1-\lambda_r)+\alpha\left(4(n\pi)^2-4\lambda_r(n\pi)^2+4\lambda_r^2\right)\right)e^{\lambda_r-\frac{\alpha}{2}}-16\alpha(n\pi)\left(\lambda_r^2-\alpha\lambda_r+\frac{\alpha^2}{4}+(n\pi)^2\right)e^{-\frac{\alpha}{2}}$$
$$g_2=-4(n\pi)e^{\lambda_r}\left(\alpha^3-4\alpha^2\lambda_r+\alpha\left(4\lambda_r^2+4(n\pi)^2\right)\right)+4\alpha^3(n\pi)(1+\lambda_r)-4\alpha^2(n\pi)\left(4\lambda_r+\lambda_r^2\right)+4\alpha(n\pi)\left(4(n\pi)^2+4\lambda_r(n\pi)^2+4\lambda_r^2\right)-16(n\pi)^3\lambda_r^2$$
$$\mathcal{F}=\frac{Sh^2}{48D\alpha\lambda_r(n\pi)\left(4\lambda_r^2-4\alpha\lambda_r+\alpha^2+4(n\pi)^2\right)} \quad (71)$$

According to previous equations, the shape function of the free vibration of the beam about its buckled configuration can be written as follows:

$$\psi(X)=C_1e^{\lambda_1X}+C_2e^{\lambda_2X}+C_3e^{\lambda_3X}+C_4e^{\lambda_4X}+C_5\nabla^2\eta(X) \quad (72)$$

To determine the natural frequencies and the five constants C_r, a procedure is applied. First, Eq. (69) is substituted into Eq. (72) to give the shape function $\psi(X)$ in the form:

$$\psi(X)=\sum_{r=1}^4\left(e^{\lambda_rX}-\frac{a_r}{\omega^2+\mathcal{H}}\nabla^2\eta(X)\right)C_r \quad (73)$$

Then, Eq. (73) is substituted into the boundary conditions (Eq. (59)), which gives a system of four equations:

$$\sum_{r=1}^4 C_r=0$$
$$\sum_{r=1}^4 C_r\left(\lambda_r^2-\frac{a_r}{\omega^2+\mathcal{H}}\nabla^4\eta(0)\right)=0$$
$$\sum_{r=1}^4 C_re^{\lambda_r}=0$$
$$\sum_{r=1}^4 C_r\left(\lambda_r^2e^{\lambda_r}-\frac{a_r}{\omega^2+\mathcal{H}}\nabla^4\eta(1)\right)=0 \quad (74)$$

The postbuckling natural frequencies can be then determined by solving the following equation (Eq. (75) above).

Solving the first three equations in Eq. (74) gives the constants, C_r, in the form:

$$C_4=-C_1\frac{\delta_1}{\delta_2}$$
$$C_3=-\frac{1}{q_3-q_2}(C_4(q_4-q_2)+C_1(q_1-q_2)) \quad (76)$$
$$C_2=-C_1-C_3-C_4$$
$$\delta_1=e^{\lambda_1}-e^{\lambda_2}+\left(\frac{q_1-q_2}{q_3-q_2}\right)\left(e^{\lambda_2}-e^{\lambda_3}\right)$$
$$\delta_2=e^{\lambda_4}-e^{\lambda_2}+\left(\frac{q_4-q_2}{q_3-q_2}\right)\left(e^{\lambda_2}-e^{\lambda_3}\right) \quad (76)$$

where

$$q_r=\lambda_r^2-\frac{a_r}{\omega^2+\mathcal{H}}\nabla^4\eta(0)$$

Then, C_5 can be determined by substituting the obtained constants into Eq. (69).

It follows from Eqs. (75) and (76) that the postbuckling natural frequencies and mode shapes of simply supported beams with rough surfaces depend on the applied axial load and the surface roughness of the beam (see Eqs. (71) and (43)). According to Eq. (69), different cases can be considered. In case $\omega^2+\mathcal{H}\neq 0$, the postbuckling mode shape is a combination of the homogeneous mode shape $\psi_h(X)$ (as defined in Eq. (63)) and the particular mode shape $\psi_P(X)$ (as defined in Eq. (65)). In case $\omega^2+\mathcal{H}\to 0$, $C_5\to\infty$, and the postbuckling mode shape only depends on the particular mode shape such that:

$$\psi(X)=\nabla^2\eta(X) \quad (77)$$

Thus, a certain mode shape is expected to exhibit the special mode shape expressed in Eq. (77).

When the measures of the surface roughness are eliminated (i.e. $R_a\to 0$ and $R_S\to 0$), Eq. (75) gives the postbuckling frequencies of simply supported beams depending on only the homogeneous part of the mode shape function. According to Eqs. (70), (71) and (76), $\lim_{\alpha\to 0}\sum_{r=1}^4 a_rC_r=0$, and hence $C_5=0$. Thus, all the mode shapes are homogeneous and do not depend on the applied axial load. Therefore, the postbuckling mode shape of a simply supported beam do not exhibit the special mode shape defined in Eq. (77), as long as the surface roughness effects are neglected. These observations completely agree with the previous demonstrations by Nayfeh and Emam (2008).

4. Results and discussion

Here, the derived exact solutions of the developed model are used to investigate the surface roughness-dependence of buckling of beams. Surface roughness effects on the buckling strength, buckling configurations, and postbuckling characteristics of rough beams are discussed. The validity of the developed model and the derived solutions to capture these effects can be demonstrated by the logical reduction of the model into the classical one with the increase in the beam thickness. For instance, the limit of the critical buckling load as defined in Eq. (41) when $\alpha \to 0$ and $B \to 0$ gives the critical buckling load of the classical model Nayfeh and Emam, 2008; Shaat and Abdelkefi, 2018). In addition, the beam configurations for the different buckling modes as presented in Eqs. (42)–((44) recover the ones of the classical model (Nayfeh and Emam, 2008; Shaat and Abdelkefi, 2018) when $\alpha \to 0$ and $B \to 0$.

4.1. Buckling strength of rough nanobeams

The buckling strength of a beam structure is defined as the minimum axial compressive load required to initiate the beam buckling. According to Eq. (41), the buckling strength of the beam can be determined as the critical buckling load of the first buckling configuration ($n = 1$), as follows:

$$P_{cr} = \frac{D\pi^2}{L^2} + \frac{D\alpha^2}{4L^2} - B \tag{78}$$

It follows from Eq. (78) that the buckling strength of the beam depends on the beam surface roughness. Therefore, the surface roughness-dependence of the buckling strength of nanobeams is analyzed here.

In Fig. 2, we depict the surface roughness-dependence of the beam buckling strength where the normalized critical buckling load ($\bar{P}_{cr} = \frac{12P_{cr}L^2}{\pi^2 Ebh^3}$) when $n = 1$ is plotted as a function of the average slope of the surface roughness (R_S) and the average surface roughness (R_a). The buckling strength increases due to the beam surface roughness. The buckling strength (i.e., the critical buckling load of the first buckling configuration) increases as either R_a or R_S increases. Whereas the stiffness parameter B is subtracted (see Eq. (78)), the overall critical buckling load increases due to surface roughness. To explain this, the variations of the terms of Eq. (78) are depicted in Fig. 3. It is clear that the term ($D\alpha^2/4L^2$) is generally larger than B for all values of the surface parameters R_S and R_a. Thus, the net value of $D\alpha^2/4L^2 - B > 0$, and the critical buckling load generally increases due to surface roughness.

The rate of increase in the buckling strength of the beam due to an increase in the average surface roughness (R_a) is higher than the one due to an increase in the average slope of the surface roughness (R_S). For instance, the buckling strength of a beam with 20 nm thickness achieves ~ 27% increase when $R_a = 1$ nm (Fig. 2(a)) and ~ 9% increase when $R_a = 10$ nm due to an increase in $R_S L = 0 \to 10$ nm (Fig. 2(b)). On the other hand, the increase in $R_a = 0 \to 4$ nm causes ~ 230% and ~ 191% increases in the buckling strength of the 20 nm thick beam when $R_S L = 1$ nm and $R_S L = 10$ nm, respectively. The higher contribution of R_a over R_S can be attributed to the dependency of the beam stiffness (D) on R_a only. As depicted in Fig. 3, the parameter $D\alpha^2/4L^2$ significantly increases as R_a increases. According to Eq. (78), the stiffness D is proportionally related to the critical buckling load P_{cr}.

It follows from Fig. 2 that the decrease in the beam thickness gives more rigidity to the beam to withstand compressive loads without buckling. The nondimensional critical buckling load increases due to a decrease in the beam thickness (Fig. 2). In addition, the rate of increase in the nondimensional critical buckling load decreases as the beam thickness increases. This behavior can be attributed to the increase in contribution of the surface roughness to buckling behavior of the beam as the size decreases.

The results presented in Fig. 2 agree with observations of the beam buckling in the literature. It follows from Fig. 2(c) and (d) that the nondimensional buckling strength of the beam reduces to the one of the classical model (i.e., is $\bar{P}_{cr} = 1$ (Nayfeh and Emam, 2008)) when the surface roughness is relatively small compared to the beam size. In addition, it follows from Fig. 2(e) that the nondimensional buckling strength strongly depends on the beam size. The experiments in the literature revealed that Euler's buckling equation, $P_{cr} = D\pi^2/L^2$, gives wrong estimations of the buckling of nanowires (Hsin et al., 2008; Chang and Chang, 2010). This has been attributed to the nanowire surface stress in various studies (Shaat and Abdelkefi, 2016b; Wang and Feng, 2009). Here, we demonstrate that the discrepancies between Euler's buckling equation and the experimental results would be, as well, because of the surface roughness.

4.2. Surface roughness effects on buckling configurations of nanobeams

Here, we explore surface roughness effects on the various buckling configurations of nanobeams. The deflection of the beam ($\eta_n(X)$) of the first two buckling configurations ($n = 1$ and 2) measured at two different locations ($X = 0.5$ when $n = 1$ and $X = 0.25$ when $n = 2$) as a function of the applied compressive load is plotted in Fig. 4. In Fig. 5, the beam deflection of the first two buckling configurations at the same locations is plotted as a function of the surface roughness parameter Q where $R_a = Q$ and $R_S = Q/L$. In Fig. 6, the first four buckling configurations ($\eta_1(X) \to \eta_4(X)$) of a 20 nm thick beam are portraited for different values of the average slope of the surface roughness (R_S).

The beam exhibits no buckling when subjected to a load lower than the critical buckling load that defines the beam buckling strength (see Fig. 4(a)). When the beam is subjected to a compressive load that is slightly higher than the beam buckling strength (the buckling strength was defined in Eq. (78)), the first buckling configuration is activated, and the beam is bowed as shown in the inset of Fig. 4(a). Then, an increase in the applied compressive load causes an increase in the beam deflection and curvature. For this case, the higher-buckling modes will not be activated even if the applied load exceeds their corresponding critical buckling load values. Instead, the beam would continue to deform exhibiting the same buckling configuration but with a higher amplitude.

The 2nd buckling configuration is activated if an unbuckled beam is subjected to a load that is slightly higher than $P_{cr} = D(4\pi^2 + \frac{\alpha^2}{4})/L^2 - B$ (Fig. 4(b)). The increase in the applied compressive load, then, increases the deflection and curvature of the beam.

The surface roughness contributes to the beam buckling strength with different mechanisms. Thus, the surface roughness fosters the strength of the beam to support compressive loads. The first mechanism is the increase in the beam bending rigidity (D) due to an increase in the average surface roughness (R_a) (see Eq. (21)). As shown in Figs. 4 and 5, the beam deflection decreases due to a surface roughness increase indicating an enhanced bending rigidity. The contribution of the surface roughness to the beam bending rigidity increases as the beam thickness decreases. As shown in Fig. 5, the deflection of a 20 nm thick beam decreases to zero faster than a beam with a larger thickness. These findings are consistent with the increase in the beam buckling strength observed in Fig. 2.

Another mechanism that influences the beam strength to support compressive loads is the buckling mode localization. It can be observed that curves plotted in Fig. 4 (b) would intersect. The obtained curve when $Q = 2$ nm intersects to the curve obtained when $Q = 0$. This behavior indicates that the conventional 2nd buckling configuration is distorted because of the surface roughness. To explain this phenomenon, the first four buckling configurations are depicted for different values of the average slope of the surface roughness (R_S) in Fig. 6. When $R_S = 0$, the buckling of the beam is

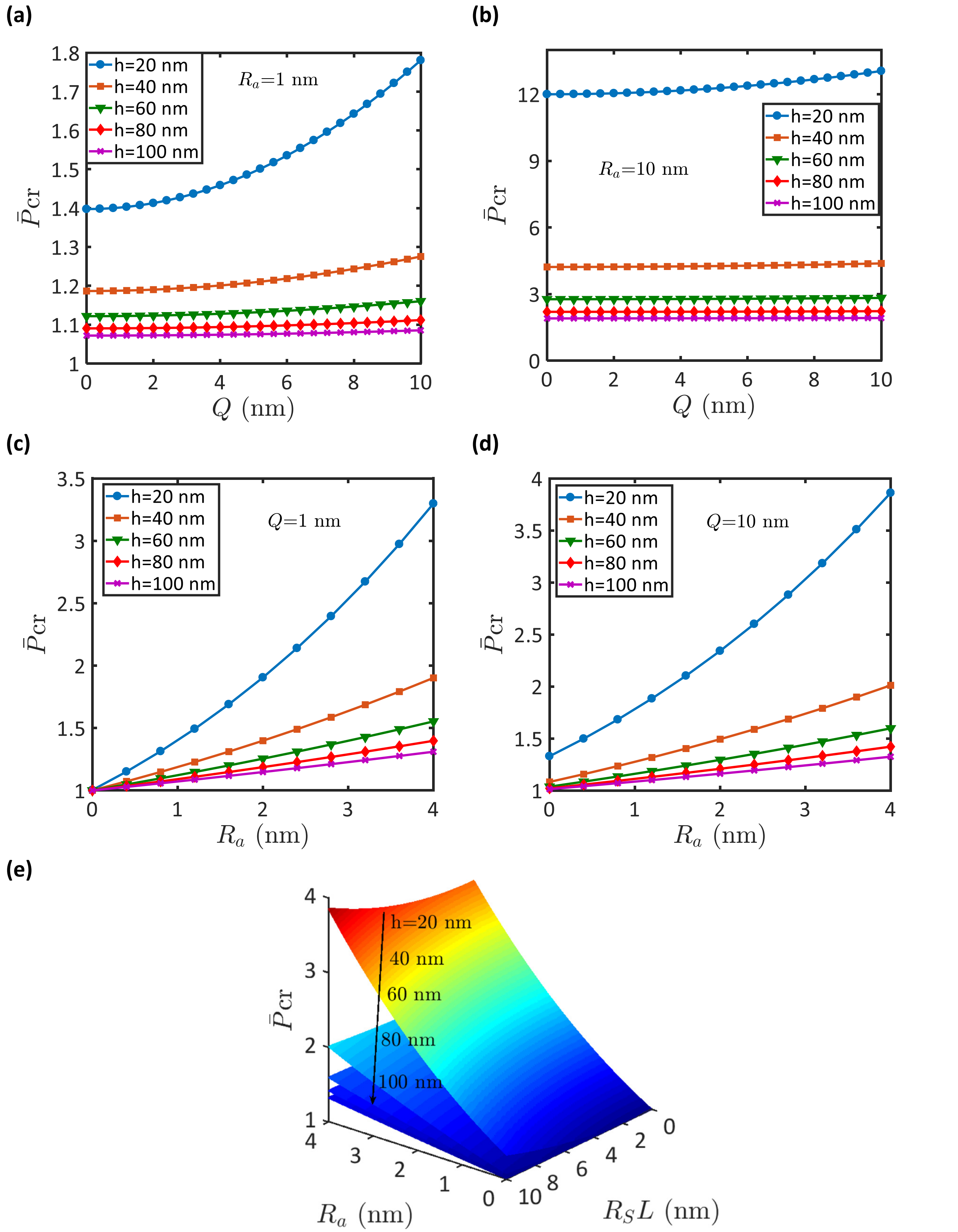

Fig. 2. Surface roughness-dependence of the buckling strength of nano-beams. (a) and (b) the nondimensional critical buckling load $\bar{P}_{cr} = \frac{12P_{cr}L^2}{\pi^2 Ebh^3}$ when $n = 1$ as a function of the average slope of the surface roughness ($R_S = Q/L$) when $R_a = 1$ nm (a) and $R_a = 10$ nm (b). (c) and (d) the nondimensional critical buckling load $\bar{P}_{cr} = \frac{12P_{cr}L^2}{\pi^2 Ebh^3}$ when $n = 1$ as a function of the average slope of the surface roughness (R_a) when $Q = 1$ nm (c) and $Q = 10$ nm (d) where $R_S = Q/L$. (e) A 3D representation of effects of R_a and R_S on $\bar{P}_{cr}$.

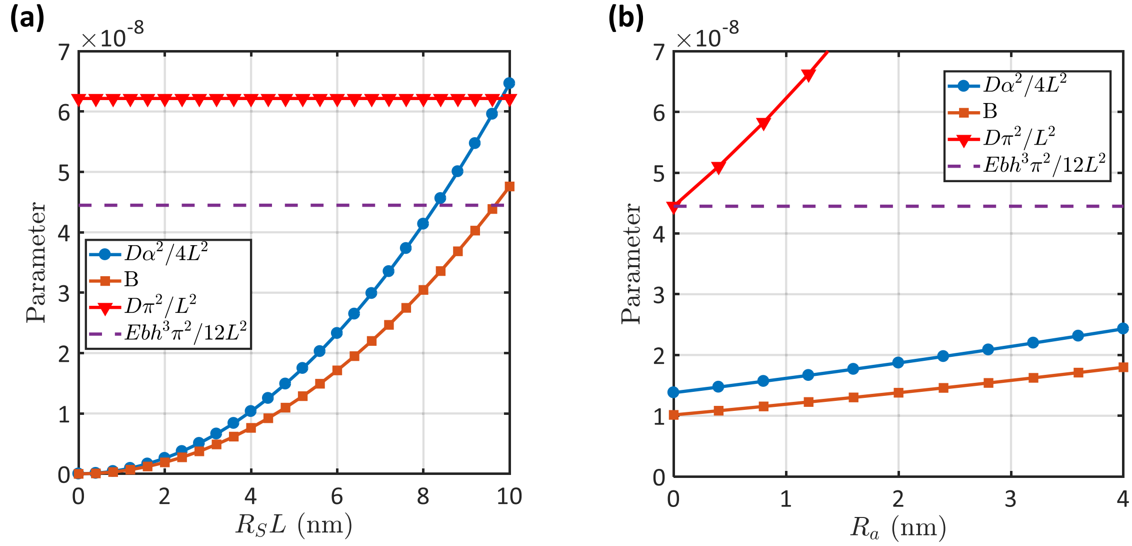

Fig. 3. Terms of the critical buckling load of the first buckling configuration (i.e., buckling strength) as defined in Eq. (78) for different values of the (a) average slope of the surface roughness (R_S) and (b) the average surface roughness (R_a). The critical buckling load of classical beams ($Ebh^3\pi^2/12L^2$) is represented by a dashed line.

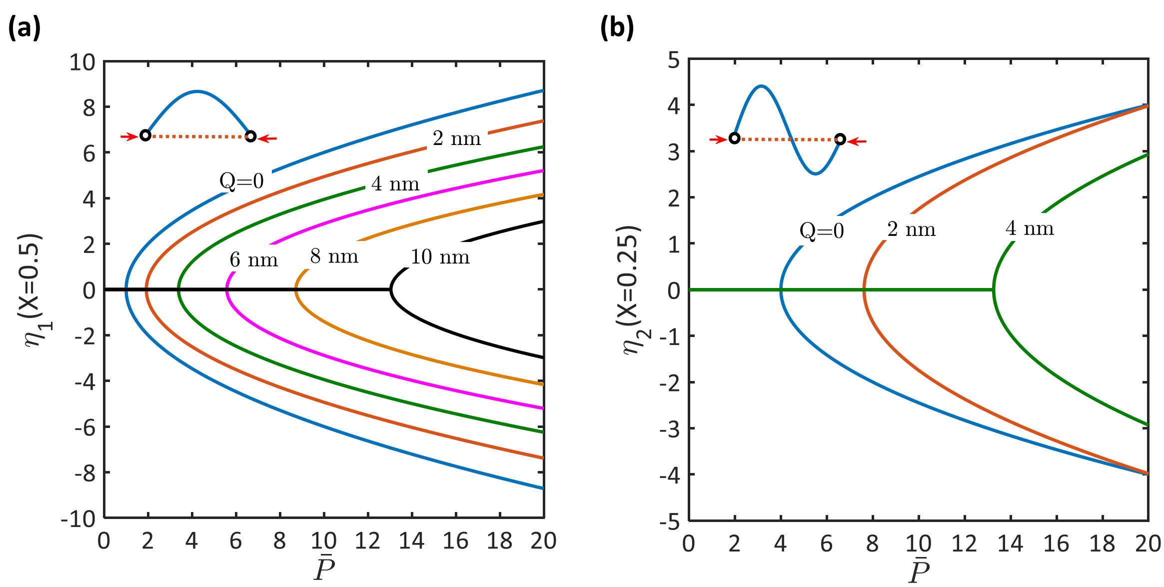

Fig. 4. Surface roughness effects on the buckling configuration of the beam. The maximum beam deflections $\eta_n(X)$ of (a) the 1st buckling configuration, $\eta_1(0.5)$ and (b) the 2nd buckling configuration, $\eta_2(0.25)$ as functions of the nondimensional compressive load ($\bar{P} = \frac{12PL^2}{\pi^2 Ebh^3}$). The results are represented for a beam with a thickness $h = 20$ nm considering different surface textures of the beam where $R_a = Q$ and $R_S = Q/L$.

distributed over the beam length. However, the beam buckling is localized within a portion of the beam due to surface roughness. Thus, the conventional buckling configuration is distorted, and the beam exhibits a localized buckling configuration. It is clear that the buckling localization increases as the average slope of the surface roughness increases. Because of the buckling mode localization, the buckling strength of the beam increases. According to Eq. (78), short beams are stronger than long ones to support compressive loads. Because of the localization, the buckling energy is confined over a small portion of the beam, and the effective length of the beam is reduced to give a stronger beam.

4.3. Surface roughness effects on the free vibration of unbuckled nanobeams

Surface roughness effects on the free vibration of simply supported unbuckled nanobeams are interpreted. The first four natural frequencies of the vibration of unbuckled nanobeams (prebuckling natural frequency) are depicted as functions of the applied compressive load in Fig. 7. A beam subjected to a load lower than its buckling strength freely oscillates about its static-straight configuration when exposed to an initial disturbance. The prebuckling frequency decreases due to an increase in the applied compressive load, as shown in Fig. 7. When the beam is loaded by its buckling strength, it loses stability where it buckles due to a small disturbance. The fundamental natural frequency of the latter case is zero, as shown in Fig. 7.

The prebuckling frequency increases due to surface roughness. This can be attributed to the increase in the beam bending rigidity due to an increase in the average surface roughness (R_a). In addition to R_a, the average slope of the surface roughness (R_S) influences the frequencies of unbuckled beams where it causes mode localization. Investigations on the mode localization of straight beams can be found in Shaat (2018b).

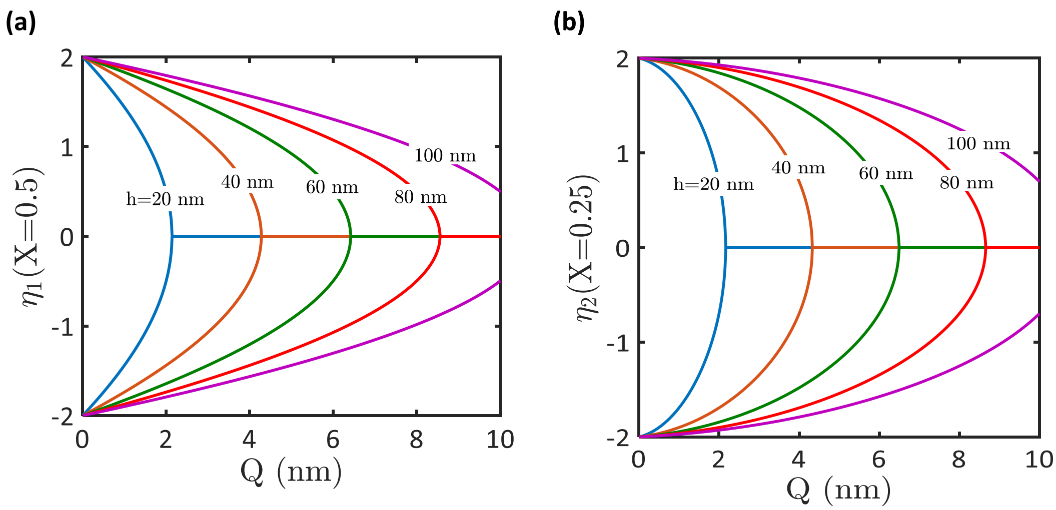

Fig. 5. Surface roughness effects on the buckling configuration of the beam. The maximum beam deflections of (a) the 1st buckling configuration, $\eta_1(0.5)$, when $\bar{P} = 2$ and (b) the 2nd buckling configuration, $\eta_2(0.25)$, when $\bar{P} = 8$ as functions of Q where $R_a = Q$ and $R_S = Q/L$.

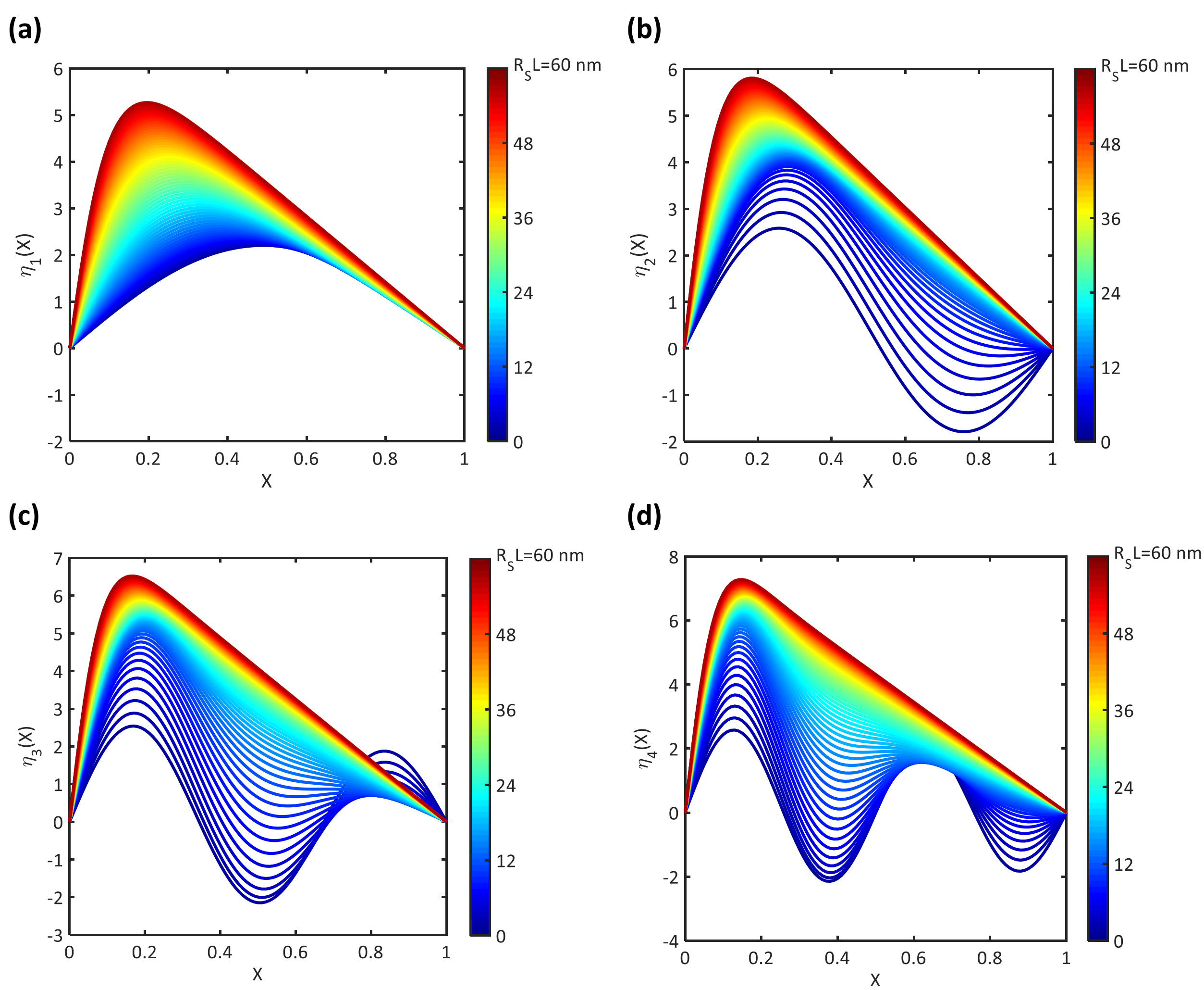

Fig. 6. Surface roughness effects on the buckling configurations of the beam. The first four buckling configurations of a beam with a thickness $h = 20$ nm for different average slope of the surface roughness R_S. The applied compressive load is equals the double of the critical buckling load of the corresponding configuration (i.e. $\bar{P} = 2\bar{P}_{cr}$). $R_a = 1$ nm.

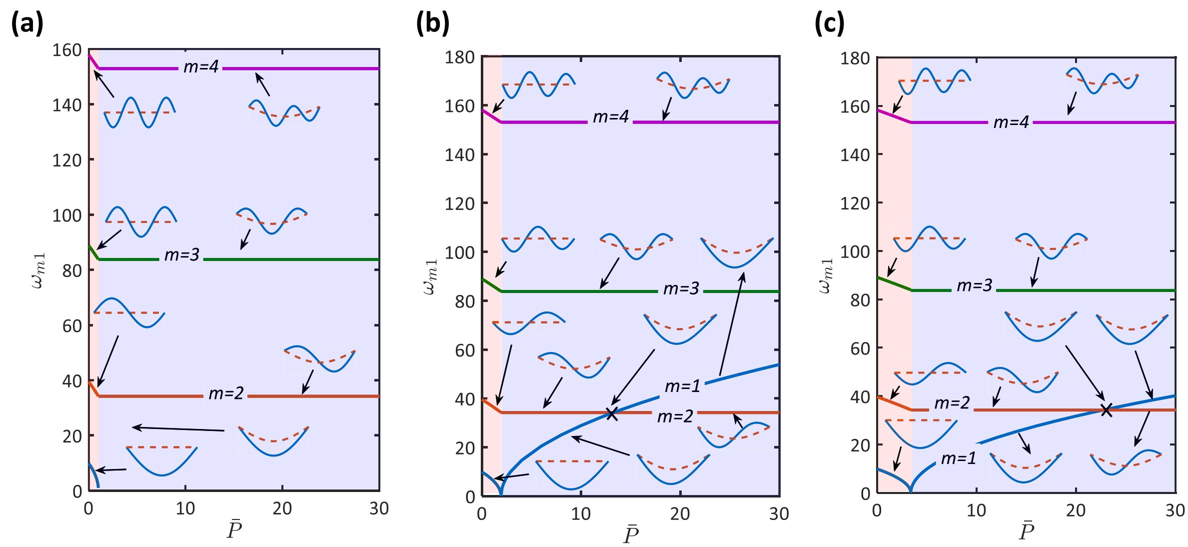

Fig. 7.. Surface roughness effects on the natural frequencies of the beam. The variations of the first four prebuckling and postbuckling natural frequencies of the first buckling configuration (ω_{m1}) as functions of the nondimensional compressive load ($\bar{P} = \frac{12PL^2}{\pi^2 Ebh^3}$) when (a) $Q = 0$, (b) $Q = 2$ nm, and (c) $Q = 4$ nm where $R_a = Q$ and $R_S = Q/L$. The red highlight refers to natural frequencies of the prebuckling regime while the blue highlight refers to the postbuckling regime. The insets are the mode shapes at different values of the nondimensional compressive load.

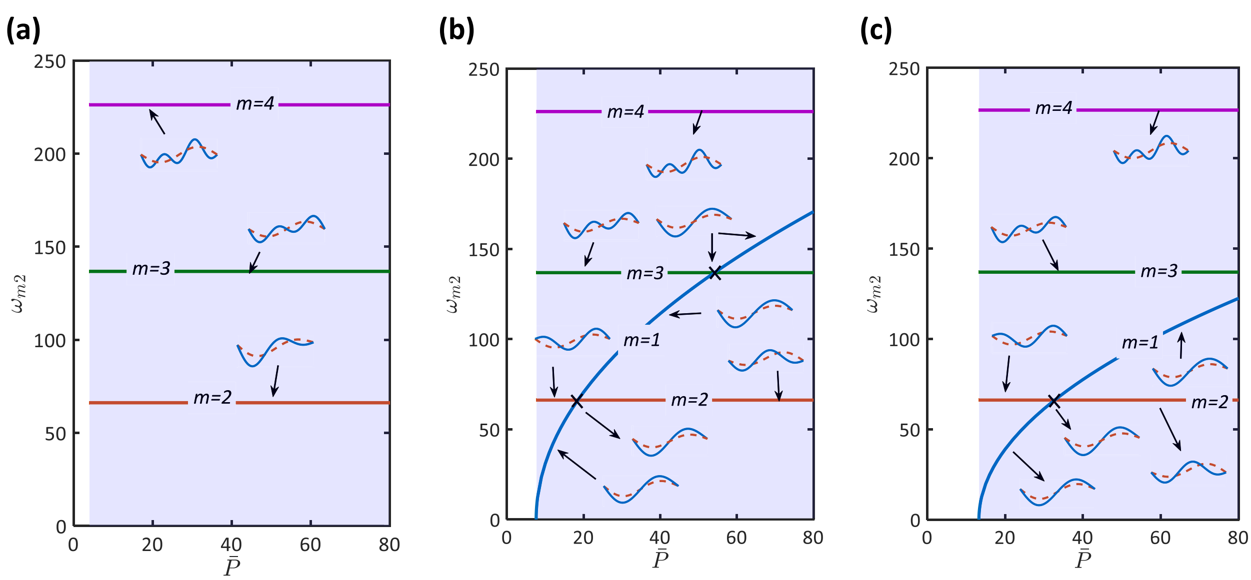

Fig. 8. Surface roughness effects on the natural frequencies of the beam. The variations of the first four postbuckling natural frequencies of the second buckling configuration (ω_{m2}) as functions of the nondimensional compressive load ($\bar{P} = \frac{12PL^2}{\pi^2 Ebh^3}$) when (a) $Q = 0$, (b) $Q = 2$ nm, and (c) $Q = 4$ nm where $R_a = Q$ and $R_S = Q/L$. The blue highlight refers to the postbuckling regime. The insets are the mode shapes at different values of the nondimensional compressive load.

4.4. Surface roughness effects on postbuckling characteristics of nanobeams: postbuckling mode shape distortion and inversion

Here, new insights into the postbuckling behavior of simply supported beams are revealed. We explore in Figs. 7–10 the variations of the postbuckling natural frequencies and mode shapes of simply supported nanobeams due applied axial load and surface roughness changes. In general, the postbuckling mode shape is a combination of the homogeneous mode shape $\psi_h(X)$ and the particular mode shape $\psi_P(X)$, according to Eq. (73).

When the surface roughness parameters are completely eliminated (i.e. $R_a \to 0$ and $R_S \to 0$), the postbuckling mode shape only depends on the homogeneous solution (i.e. $C_5 = 0$). A homogeneous postbuckling mode shape works independently of the applied compressive load (Nayfeh and Emam, 2008) (see Figs. 7(a) and 8(a)). It follows from Figs. 7(a) and 8(a) that the postbuckling mode shape is homogeneous when $Q = 0$ (where $R_a = Q$ and $R_S = Q/L$), where the natural frequencies are constants and do not vary by a change in the applied compressive load. In this case, the first postbuckling natural frequency vanishes, and the lowest apparent frequency is the second mode frequency ($\omega_{21} = 34.19$ (Fig. 7(a)) and $\omega_{22} = 66.21$ (Fig. 8(a))). The disappearance of the first mode frequency is due to the fact that the beam exhibits a snap-through motion at an infinite frequency between the two stable buckling positions (*see Supplementary Information - S1*). This behavior is guaranteed as long as the beam rotates with no friction at the supports (the first mode frequency would appear for a simply supported beam due to a friction at the support). It should be mentioned that for beams with one(two) end(s) is(are) fixed, the first mode frequency appears (Nayfeh and Emam, 2008). A fixed support inhibits the local-free rotation of the beam at the support,

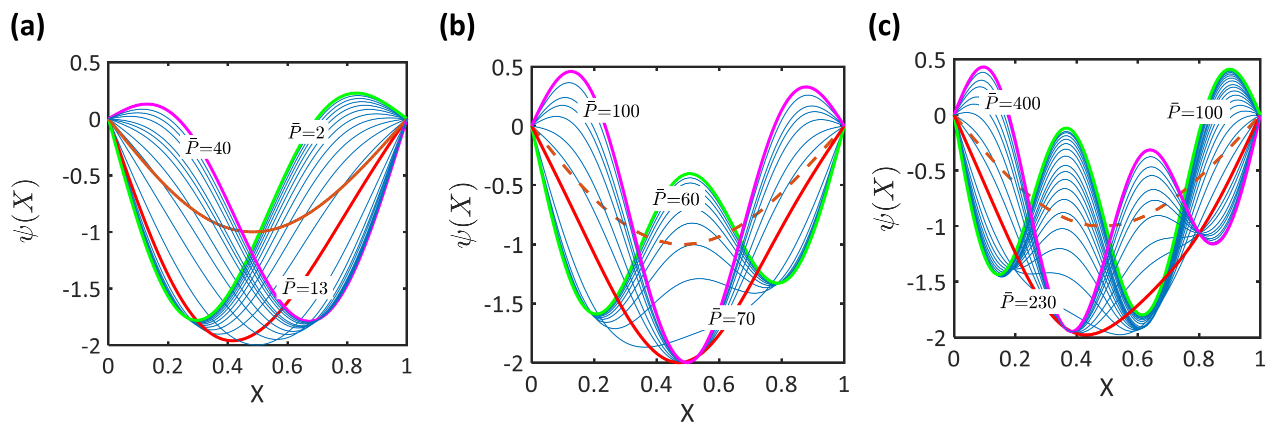

Fig. 9. Postbuckling mode shape inversion. The inversion of the (a) 2nd, (b) 3rd, and (c) 4th mode shapes of a rough beam exhibits a first buckling configuration ($n = 1$) with the increase in the nondimensional compressive load ($\bar{P}$). The original postbuckling mode shape and its inverted shape are highlighted. In addition, the transition between the inverted mode shapes is red highlighted where the beam exhibits the special mode shape defined in Eq. (77) ($\psi(X) = \nabla^2\eta(X)$). $h = 20$ *nm* and $Q = 2$ nm where $R_a = Q$ and $R_S = Q/L$.

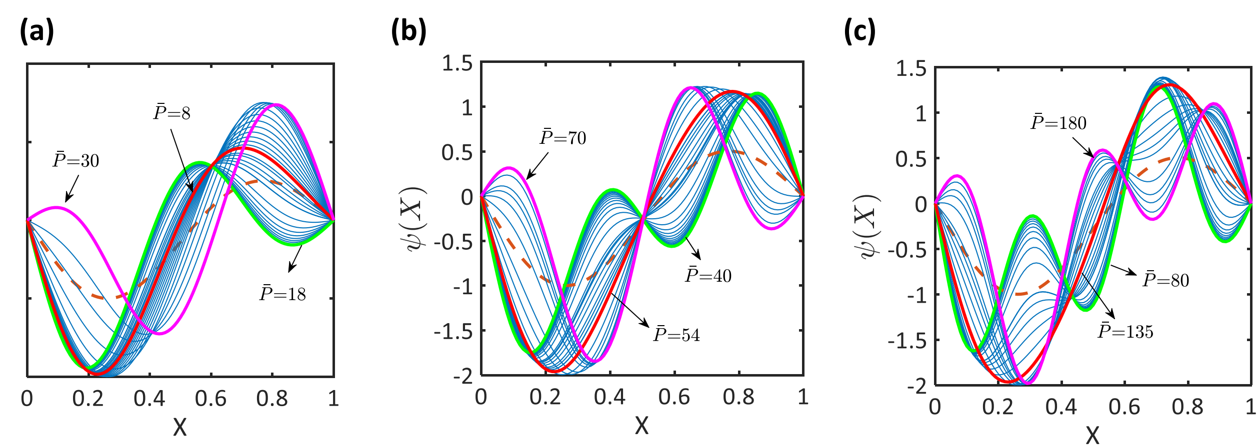

Fig. 10. Postbuckling mode shape inversion. The inversion of the (a) 2nd, (b) 3rd, and (c) 4th mode shapes of a beam exhibits a second buckling configuration ($n = 2$) with the increase in the nondimensional compressive load ($\bar{P}$). The original postbuckling mode shape and its inverted shape are highlighted. In addition, the transition between the inverted mode shapes is red highlighted where the beam exhibits the special mode shape defined in Eq. (77) ($\psi(X) = \nabla^2\eta(X)$). $h = 20$ nm and $Q = 2$ nm where $R_a = Q$ and $R_S = Q/L$.

and hence the beam elastically vibrates about its stable buckling position.

The postbuckling mode shapes are axial load-dependents due to surface roughness. Surface roughness inhibits the snap-though motion of the beam, and hence it elastically vibrates around a stable buckling position. When $R_a > 0$ and $R_S > 0$, $C_5 \neq 0$ and the beam exhibits a special mode of vibration defined in Eq. (77). This mode is identical to the buckling configuration of the beam but with a different amplitude. The corresponding natural frequency of this mode ($\omega = \sqrt{-\mathcal{H}}$) increases as the applied axial load increases, as shown in Figs. 7(b), (c) and 8(b), (c). The existence of this mode for simply supported beams can be attributed to the coupling term ($\alpha\nabla^3 W(X,T)$) in the equation of motion, which depends mainly on the average slope of the surface roughness (R_S). The natural frequency of this mode decreases due to an increase in the average slope of the surface roughness (R_S). The natural frequencies of the other modes of vibration slightly change due to a change in either the applied axial load value or the beam surface roughness.

In Figs. 7–10, we reveal the postbuckling mode shape inversion due to surface roughness, for the first time. Whereas the postbuckling mode shapes of simply supported-classical beams are independent of the applied axial load, these modes of a simply supported rough beam are inverted as the applied axial load increases. As shown in Figs. 9 and 10, a postbuckling mode shape is distorted as the applied axial load increases (*see Supplementary Information - S2*). The postbuckling mode is attracted to the special first postbuckling mode (Eq. (77)) as the applied axial load approaches a value at which the frequency of the considered mode equals $\sqrt{-\mathcal{H}}$. The intersection points defined in Figs. 7(b), (c) and 8(b) and (c) identify the applied axial load value at which the beam exhibits the special first postbuckling mode (Eq. (77)). Beyond this value of the applied axial load, the postbuckling mode shape restores an inverted shape of the original mode shape, as shown in Figs. 7–10 and Supplementary Information - S2.

5. Conclusions

In this study, we revealed new buckling phenomena of beams due to their surface roughness. These phenomena are clearly seen as long as the beam size is lower than a critical value below which the contribution of the surface roughness to the buckling behavior of the beam is significant.

It is concluded that surface roughness fosters the beam ability to withstand compressive loads. The buckling strength value, which was defined by the lowest compressive load value required to buckle the beam, was found to increase due to surface roughness. The average surface roughness (R_a) provides more rigidity to the beam against compressive loads, and the average slope of the surface roughness (R_S) enhances the buckling mode localization. We demonstrated that a conventional buckling configuration would be distorted, and the beam would exhibit a localized buckling configuration. The buckling energy is confined over a small portion of a beam exhibits the localized buckling configuration resulting in an increase in the rigidity and strength.

It has been acknowledged previously that the postbuckling mode shape of simply supported ideal beams (beams with no surface roughness) is homogeneous and load-independent (Nayfeh and Emam, 2008). Here, we revealed a general postbuckling mode shape of simply supported rough beams that depends on the applied compressive load. We presented the evolution of the postbuckling mode shape with the applied load increase. The postbuckling mode shape was observed distorted due to surface roughness. It was observed that, as long as the applied axial load is of a value at which the postbuckling frequency equals $\sqrt{-\mathcal{H}}$, the postbuckling mode shape is completely distorted, and the beam exhibits a mode shape that is identical to its buckling configuration but with a different amplitude ($\nabla^2\eta(X)$). Beyond the aforementioned axial load value, the postbuckling mode shape starts to exhibit an inverted form of its original shape. Thus, at high load values, the postbuckling mode shape is completely inverted.

The findings presented in this study highlight the influence of surface roughness on the buckling characteristics of micro/nanobeams. These findings are important to design beams with surface textures for advanced buckling applications.

Author Contributions

M. Shaat conceived the idea and developed the model and the analytical solutions. The model and solutions were revised and discussed by S. Emam. The presented results were prepared by M. Shaat and S. Faroughi and discussed by S. Emam, M. Shaat, and U. Javed. All authors wrote the manuscript.

Data for reference

The data that support the findings of this study are included in the article. Any further requested information can be addressed to the corresponding author.

Declaration of Competing Interest

The authors declare that they have no known competing financial interests or personal relationships that could have appeared to influence the work reported in this paper.

Acknowledgements

This research is supported by Abu Dhabi University - United Arab Emirates (Grants 19300474 and 19300475).

Supplementary materials

Supplementary material associated with this article can be found, in the online version, at doi:10.1016/j.ijsolstr.2020.03.007.

References

Akgöz, B., Civalek, Ö, 2011. Strain gradient elasticity and modified couple stress models for buckling analysis of axially loaded micro-scaled beams. Int. J. Eng. Sci. 49, 1268–1280.
Allahyari, E., Fadaee, M., 2016. Analytical investigation on free vibration of circular double-layer graphene sheets including geometrical defect and surface effects. Compos. Part B 85, 259–267.
Aydogdu, M., Arda, M., 2016. Torsional vibration analysis of double walled carbon nanotubes using nonlocal elasticity. Int. J. Mech. Mater. Des. 2 (1), 71–84.
Chaht, F.L., Kaci, A., Houari, M.S.A., Tounsi, A., Beg, O.A., Mahmoud, S., 2015. Bending and buckling analyses of functionally graded material (FGM) size-dependent nanoscale beams including the thickness stretching effect. Steel Compos. Struct. 18, 425–442.
Chang Jr., M.Deka, Chang, F.C., 2010. Effect of synthesis process on the Young's modulus of titanate nanowire. Phys. Status Solidi A 207 (2), 327–333.
Duan, H.L., Wang, J., Karihaloo, B.L., 2008. Theory of elasticity at the nanoscale. In: Aref, H., Van der Giessen, E. (Eds.). In: Advances in Applied Mechanics, 42. Elsevier, Amsterdam, pp. 1–68.
Eremeyev, V.A., 2016. On effective properties of materials at the nano- and microscales considering surface effects. Acta Mech. 227 (1), 29–42.
Emam, SA., 2013. A general nonlocal nonlinear model for buckling of nanobeams. Appl. Math. Model. 37 (10–11), 6929–6939.
Ghannadpour, S., Mohammadi, B., Fazilati, J., 2013. Bending, buckling and vibration problems of nonlocal Euler beams using Ritz method. Compos. Struct. 96, 584–589.
Gholami, R., Ansari, R., Rouhi, H., 2015. Studying the effects of small scale and Casimir force on the non-linear pull-in instability and vibrations of FGM microswitches under electrostatic actuation. Int. J. Non-Linear Mech. 77, 193–207.
Gupta, A., Akin, D., Bashir, R., 2004. Detection of bacterial cells and antibodies using surface micromachined thin silicon cantilever resonators. J. Vac. Sci. Technol. B 22 (6), 2785–2791.
Gurtin, M.E., Murdoch, A.I., 1975a. Addenda to our paper A continuum theory of elastic material surfaces. Arch. Ration. Mech. Anal. 59, 389–390.
Gurtin, M.E., Murdoch, A.I., 1975b. A continuum theory of elastic material surfaces. Arch. Ration. Mech. Anal. 57, 291–323.
Hsiao, H.-H., Chu, C.H., Tsai, D.P., 2017. Fundamentals and applications of metasurfaces. Small Methods 1, 1600064.
Hsin, C.-L., Mai, W., Gu, Y., Gao, Y., Huang, C.-T., Liu, Y., Chen, L.-J., Wang, Z.-L., 2008. Elastic properties and buckling of silicon nanowires. Adv. Mater. 20, 3919–3923.
Javili, A., McBride, A., Steinmann, P., 2012. Thermomechanics of solids with lower-dimensional energetics: on the importance of surface, interface, and curve structures at the nanoscale. A unifying review. Appl. Mech. Rev. 65, 010802–1–31.
Javili, A., dell'Isola, F., Steinmann, P., 2013. Geometrically nonlinear higher-gradient elasticity with energetic boundaries. J. Mech. Phys. Solids 61, 2381–2401.
Jain, A., Vaidehi, N., Rodriguez, G., 1993. A fast recursive algorithm for molecular dynamics simulation. J. Comput. Phys. 106, 258–268.
Johnson, L., Gupta, A.K., Ghafoor, A., Akin, D., Bashir, R., 2006. Characterization of vaccinia virus particles using microscale silicon cantilever resonators and atomic force microscopy. Sens. Actuators B 115, 189–197.
Kahrobaiyan, M.H., Asghari, M., Ahmadian, M.T., 2015. A strain gradient Timoshenko beam element: application to MEMS. Acta Mech. 226 (2), 505–525.
Khorshidi, MA, Shariati, M, Emam, SA, 2016. Postbuckling of functionally graded nanobeams based on modified couple stress theory under general beam theory. Int. J. Mech. Sci. 110, 160–169.
Kong, S., 2013. Size effect on pull-in behavior of electrostatically actuated microbeams based on a modified couple stress theory. Appl. Math. Model. 37 (12–13), 7481–7488.
Laplace, P.S., 1805. Sur l'action capillaire. supplément à la théorie de l'action capillaire. In: Traité de mécanique céleste, 4. Supplement 1, Livre X. Gauthier–Villars et fils, Paris, pp. 771–777.
Laplace, P.S., 1806. À la théorie de l'action capillaire. supplément à la théorie de l'action capillaire. In: Traité de mécanique céleste, 4. Supplement 2, Livre X. Gauthier–Villars et fils, Paris, pp. 909–945.
Lazopoulos, K.A., Lazopoulos, A.K., 2010. Bending and buckling of thin strain gradient elastic beams. Eur. J. Mech. 29, 837–843.
Li, L, Hu, Y., 2015. Buckling analysis of size-dependent nonlinear beams based on a nonlocal strain gradient theory. Int. J. Eng. Sci. 97, 84–94.
Liu, Y., Shah, S., Tan, J., 2012. Computational modeling of nanoparticle targeted drug delivery. Rev. Nanosci. Nanotechnol. 1, 66–83.
Lu, C.H., Zhang, Y., Tang, S.F., Fang, ZB, Yang, HH, Chen, X., Chen, G.N., 2012. Sensing HIV related protein using epitope imprinted hydrophilic polymer coated quartz crystal microbalance. Biosens. Bioelectron. 31 (1), 439–444.
Lurie, S., Belov, P., 2014. Gradient effects in fracturemechanics for nano-structured materials. Eng. Fract. Mech. 130, 3–11.
Madeo, A., Neff, P., 2017. Dispersion of waves in micromorphic media and metamaterials. In: Voyiadjis, G. (Ed.), Handbook of Nonlocal Continuum Mechanics for Materials and Structures. Springer, Cham.
Madeo, A., Neff, P., Ghiba, I.D, Placidi, L., Rosi, G., 2015. Wave propagation in relaxed micromorphic continua: modeling metamaterials with frequency band–gaps. Contin. Mech. Thermodyn. 27 (4–5), 551–570.
Mindlin, R., 1964. Microstructure in linear elasticity. Arch. Ration. Mech. Anal. 16, 51–78.
Mohammad-Abadi, M., Daneshmehr, A.R., 2014. Size dependent buckling analysis of microbeams based on modified couple stress theory with high order theories and general boundary conditions. Int. J. Eng. Sci. 74, 1–14.
Najar, F., El-Borgi, S., Reddy, J., Mrabet, K., 2015. Nonlinear nonlocal analysis of electrostatic nanoactuators. Compos. Struct. 120, 117–128.
Nateghi, A., Salamat-talab, M., Rezapour, J., Daneshian, B., 2012. Size dependent buckling analysis of functionally graded micro beams based on modified couple stress theory. Appl. Math. Model. 36, 4971–4987.
Nayfeh, A.H., Emam, S.A., 2008. Exact solution and stability of postbuckling configurations of beams. Nonlinear Dyn. 54, 395–408.
Nejad, M.Z., Hadi, A., Rastgoo, A., 2016. Buckling analysis of arbitrary two-directional functionally graded Euler–Bernoulli nano-beams based on nonlocal elasticity theory. Int. J. Eng. Sci. 103, 1–10.
Niknam, H, Aghdam, M., 2015. A semi analytical approach for large amplitude free vibration and buckling of nonlocal FG beams resting on elastic foundation. Compos. Struct. 119, 452–462.

Palasantzas, G., 2007. Random surface roughness influence on gas damped nanoresonators. Appl. Phys. Lett. 90 (4).
Podio-Guidugli, P., Caffarelli, G.V., 1990. Surface interaction potentials in elasticity. Arch. Ration. Mech. Anal. 109, 345–385.
de Poisson, S.D., 1831. Nouvelle théorie de l'action capillaire. Bachelier Père et Fils, Paris.
Povstenko, Y., 2013. Mathematical modeling of phenomena caused by surface stresses in solids. In: Altenbach, H., Morozov, N.F. (Eds.), Surface Effects in Solid Mechanics. Springer, Berlin, pp. 135–153.
Rahaeifard, M., Kahrobaiyan, M.H., Asghari, M., Ahmadian, M.T., 2011. Static pull-in analysis of microcantilevers based on the modified couple stress theory. Sens. Actuators A 171 (2), 370–374.
Rahaeifard, M., Ahmadian, M., 2015. On pull-in instabilities of microcantilevers. Int. J. Eng. Sci. 87, 23–31.
Rubin, M., Benveniste, Y., 2004. A Cosserat shell model for interphases in elastic media. J. Mech. Phys. Solids 52, 1023–1052.
Sedighi, H.M., Daneshmand, F., Abadyan, M., 2015. Modeling the effects of material properties on the pull-in instability of nonlocal functionally graded nano-actuators. Z. Angew. J. Appl. Math. Mech. 96 (3), 385–400.
Shaat, M., Mahmoud, F.F., Alshorbagy, A.E., Alieldin, S.S., Meletis, E.I., 2012. Size-dependent analysis of functionally graded ultra-thin films. Struct. Eng. Mech. 44 (4), 431–448.
Shaat, M., Abdelkefi, A., 2016a. Modeling of mechanical resonators used for nanocrystalline materials characterization and disease diagnosis of HIVs. Microsyst. Technol. 22 (2), 305–318.
Shaat, M., Abdelkefi, A., 2016b. Reporting buckling strength and elastic properties of nanowires. J. Appl. Phys. 120, 235104.
Shaat, M., 2016b. Physical and mathematical representations of couple stress effects on micro/nanosolids. Int. J. Appl. Mech. 7 (1), 1550012–1550028.
Shaat, M., Abdelkefi, A., 2017. Material structure and size effects on the nonlinear dynamics of electrostatically-actuated nano-beams. Int. J. Non-Linear Mech. 89, 25–42.
Shaat, M, Faroughi, S., 2019. Influence of long-range interatomic and interlayer interactions on dispersion of acoustic waves by multilayer graphene. Physica E 108, 74–82.
Shaat, M., 2018a. A reduced micromorphic model for multiscale materials and its applications in wave propagation. Compos. Struct. 201, 446–454.
Shaat, M., 2018. Mode localization phenomenon of functionally graded nanobeams due to surface integrity. Int. J. Mech. Mater. Des. https://doi.org/10.1007/s10999-018-9421-x.
Shaat, M., 2018c. Effects of surface integrity on the mechanics of ultra-thin films. Int. J. Solids Struct. 136–137, 259–270.
Shaat, M., 2018d. Effects of processing force on performance of nano-resonators produced by magnetron sputtering deposition. Physica E 104, 42–48.
Shaat, M., Faroughi, S., 2018. Influence of surface integrity on vibration characteristics of microbeams. Eur. J. Mech./ASolids 71, 365–377.
Shaat, M., Abdelkefi, A., 2018. Buckling characteristics of nanocrystalline nano-beams. Int. J. Mech. Mater. Des. 1–19.
Shaat, M., Mahmoud, F.F., Gao, X.-L., Faheem, A.F., 2014. Size-dependent bending analysis of Kirchhoff nano-plates based on a modified couple-stress theory including surface effects. Int. J. Mech. Sci. 79, 31–37.
Shaat, M., Mohamed, S.A., 2014. Nonlinear-electrostatic analysis of micro-actuated beams based on couple stress and surface elasticity theories. Int. J. Mech. Sci. 84, 208–217.
Shafiei, N., Kazemi, M., 2017. Buckling analysis on the bi-dimensional functionally graded porous tapered nano-/micro-scale beams. Aerosp. Sci. Technol. 1–28.
Šilhavý, M., 2013. A direct approach to nonlinear shells with application to surface–substrate interactions. Math. Mech. Complex Syst. 1 (2), 211–232.
Simsek, M., Yurtcu, H., 2013. Analytical solutions for bending and buckling of functionally graded nanobeams based on the nonlocal Timoshenko beam theory. Compos. Struct. 97, 378–386.
Thai, H.T., 2012. A nonlocal beam theory for bending, buckling, and vibration of nanobeams. Int. J. Eng. Sci. 52, 56–64.
Wang, C., Zhang, Y., Ramesh, S.S., Kitipornchai, S., 2006. Buckling analysis of micro-and nanorods/tubes based on nonlocal Timoshenko beam theory. J. Phys. D 39, 3904.
Wu, G., Ji, H., Hansen, K., Thundat, T., Datar, R., Cote, R., Hagan, M.F., Chakraborty, A.K., Majumdar, A., 2001. Proc. Natl. Acad. Sci. USA 98, 1560.
Xing, Y., Wang, S., Feng, S., Shang, W., Deng, S., Wang, L., Hou, Y., Zheng, Y., 2017. Controlled transportation of droplets and higher fog collection efficiency on a multi-scale and multi-gradient copper wire. RSC Adv. 7, 29606.
Xu, X-J, Wang, X-C, Zheng, M-L, Ma, Z, 2017. Bending and buckling of nonlocal strain gradient elastic beams. Compos. Struct. 160, 366–377.
Yoon, H.S., Park, B., Jun, S.C., 2013. Surface roughness effects on the frequency tuning performance of a nanoelectromechanical resonator. Nanoscale Res. Lett. 8 (1), 270.
Young, T., 1805. An essay on the cohesion of fluids. Philos. Trans. R. Soc. Lond. 95, 65–87.
Wang, G.-F., Feng, X.-Q., 2009. Surface effects on buckling of nanowires under uniaxial compression. Appl. Phys. Lett. 94, 141913.
Wang, Z., Zhao, Y., 2009. Self-instability and bending behaviors of nano plates. Acta Mech. Solida Sin. 22 (6), 630–643.
Zang, Jin-Liang, Zhao, Ya-Pu, 2012. A diffusion and curvature dependent surface elastic model with application to stress analysis of anode in lithium ion battery. Int. J. Eng. Sci. 61, 156–170.